

# Recent Outbursts from the Transient X-Ray Pulsar Cep X-4 (GS 2138+56)

Colleen A. Wilson, Mark H. Finger<sup>1</sup>, D. Matthew Scott<sup>1</sup>

ES 84 Space Sciences Laboratory, NASA/Marshall Space Flight Center, Huntsville, AL 35812;  
colleen.wilson@msfc.nasa.gov, finger@gibson.msfc.nasa.gov, scott@gibson.msfc.nasa.gov

## ABSTRACT

We report on X-ray observations of the 66 s period transient X-ray pulsar Cep X-4 (GS 2138+56) with the Burst and Transient Source Experiment (BATSE) on the *Compton Gamma-Ray Observatory (CGRO)* and with the Rossi X-ray Timing Explorer (*RXTE*). Two outbursts from Cep X-4 were observed with BATSE in 1993 June-July and 1997 July. Pulse frequencies of  $\nu = 15.0941 \pm 0.0002$  mHz on 1993 June 25 (MJD 49,163) and  $\nu = 15.0882 \pm 0.0002$  mHz on 1997 July 12 (MJD 50,641) were each measured from 2 day spans of BATSE data near each outburst's peak. Cep X-4 showed an average spin down rate of  $\dot{\nu} = (-4.14 \pm 0.08) \times 10^{-14}$  Hz s<sup>-1</sup> between the 1993 and 1997 outbursts. After BATSE could no longer detect Cep X-4, public observations were performed on 1997 July 18 & 25 with the Proportional Counter Array (PCA) on *RXTE*. A pulse frequency of  $\nu = 15.088 \pm 0.004$  mHz was measured from observations on 1997 July 18 (MJD 50,647). Significant aperiodic noise, with an rms variance of  $\sim 18\%$  in the frequency range 0.01-1.0 Hz was observed on both days. Energy and intensity dependent pulse shape variations were also seen in these data. Recently published optical observations associate Cep X-4 with a Be companion star. If all 4 outbursts observed from Cep X-4 are assumed to occur at the same orbital phase, we find that the orbital period is between 23 days and 147.3 days.

*Subject headings:* pulsars: individual (Cep X-4, GS 2138+56) — stars: neutron — x-rays: stars — binaries:X-ray

---

<sup>1</sup>Universities Space Research Association

## 1. Introduction

In the last 25 years more than 40 accretion-powered X-ray pulsars have been discovered. At least half of these are transient, of which 12 have known Be star companions. Neutron stars with Be companions accrete material from the slow, dense, stellar outflow thought to be confined to the equatorial plane of the Be star. Cep X–4 has recently been associated with a Be star of magnitude  $V=14.2$  (Roche, Green, & Hoenig 1997; Argyle 1997) that lies within the *ROSAT* error circle (Schulz, Kahabka, & Zinnecker 1995). This association is based upon positional coincidence, strong H- $\alpha$  and H- $\beta$  emission lines (typical of Be/X-ray binaries), and measurement of the optical absorption column density which is in good agreement with *ROSAT* measurements. The companion is most likely a B1V-B2Ve star at a distance of  $3.8\pm 0.6$  kpc (Bonnet-Bidaud & Mouchet 1998).

Cep X–4 was discovered with *OSO-7* in 1972 June–July, but no pulsations were detected (Ulmer et al. 1973). The *Ginga* All-Sky Monitor first detected a new transient source, GS 2138+56, on 1988 March 19 at a 50 mcrab level. GS 2138+56 was later identified with Cep X–4 because it fell in the  $0.4^\circ$  error box and had a similar spectrum. Pulsations at a frequency of  $15.09457 \pm 0.00002$  mHz (MJD 47,263.5) were detected during a month long outburst which peaked at about 100 mCrab (1–20 keV) in early April 1988. The source apparently did not appear again until 1993 June when it was detected with *ROSAT* (Schulz, Kahabka, & Zinnecker 1995) and the Burst and Transient Source Experiment (BATSE) on the *Compton Gamma-Ray Observatory (CGRO)*. Near the outburst peak, pulsations at a frequency of  $15.0941 \pm 0.0002$  mHz (MJD 49,163.0) were detected with BATSE. The outburst lasted about two weeks and had a peak pulsed flux of 15–20 mCrab (20–50 keV). In 1997 July–August, BATSE and the All-Sky Monitor (ASM) on the *Rossi X-ray Timing Explorer (RXTE)* observed an outburst from Cep X–4. BATSE detected pulsations at a frequency of  $15.0882 \pm 0.0002$  mHz (MJD 50,641) near the outburst peak. This outburst lasted about 2 weeks and peaked at a pulsed flux of about 10–15 mCrab (20–50 keV). The ASM observed a longer (4 week) outburst with a peak flux of about 40 mCrab (2–12 keV). The best fit average spin-down rate is  $\dot{\nu} = (-4.1 \pm 0.4) \times 10^{-15}$  Hz s $^{-1}$  between the 1988 and 1993 outbursts. Between the 1993 and 1997 outbursts, the average spin-down rate,  $\dot{\nu} = (-4.14 \pm 0.08) \times 10^{-14}$  Hz s $^{-1}$ , is 10 times larger than the spin-down rate between the first two outbursts. Apparent spin-up observed during the first two outbursts and spin-down in the recent outburst may be intrinsic or due to binary orbital motion.

In this paper we present observations of two outbursts from Cep X–4 in 1993 and 1997. Our observations with BATSE include histories of pulse frequency, pulsed flux, and average 20–50 keV pulse profiles. We obtained public *RXTE* Proportional Counter Array (PCA) data from 1997 July 18 & 25, after BATSE stopped detecting Cep X–4. We present pulse

frequency measurements, pulse profiles, and power spectra from these data.

## 2. Observations and Analyses

### 2.1. Instruments

Three different instruments spanning energies from 2-1800 keV were used to study Cep X-4: BATSE on *CGRO*, and the PCA and ASM both on *RXTE*. BATSE consists of eight identical uncollimated detector modules positioned on the corners of the *CGRO* spacecraft such that the normal vectors of the detectors are perpendicular to the faces of a regular octahedron, providing all-sky coverage. The BATSE data presented here are taken with the large-area detectors (LADs), which are NaI(Tl) scintillation crystals with a geometric area of 2025 cm<sup>2</sup> and a thickness of 1.27 cm. The LADs are sensitive to photons from 20 to 1800 keV. Two BATSE data types were used in this analysis, the CONT (2.048 s, 16 energy channel) data and the DISCLA (1.024 s, 4 energy channel) data. A more complete description of the instrument and data types can be found in Fishman et al. (1989).

The PCA on *RXTE* consists of five proportional counters sensitive to photons from 2-60 keV and has a total collecting area of 6500 cm<sup>2</sup>. The PCA is a collimated instrument with an approximately circular field-of-view with a FWHM of about 1° (Jahoda et al. 1996). Three PCA data types were used in this analysis, Standard 1 (125 ms, no energy resolution) data, Good Xenon data (1  $\mu$ s, 256 energy channel) data, and Standard 2 (16 s, 128 channel) data. The *RXTE* ASM consists of three wide-angle shadow cameras equipped with Xenon proportional counters with a total collecting area of 90 cm<sup>2</sup>. The ASM provides 90 second images of most of the sky every 96 minutes in three energy channels from 2-12 keV (Levine et al. 1996). For this analysis we used single day averaged data from the full 2-12 keV band.

### 2.2. Techniques

Histories of pulse frequency and pulsed flux (20-50 keV) were determined on 2-day intervals of BATSE DISCLA data. Pulse frequencies were estimated from fits to data at a range of trial frequency offsets from a pulse phase model. The pulse phase model used a constant frequency,  $\nu_0$ , obtained from daily power spectra of the BATSE DISCLA data. Each 2-day interval of data were fit with a background model plus a 6 harmonic Fourier expansion in the pulse phase model to generate a pulse profile at the model frequency. The background was modeled as a quadratic spline, with segments every 300 s and with value

and slope continuous between adjacent segments. (See Bildsten et al. 1997 for a detailed description of pulsed flux and pulse frequency estimation techniques.) For each 2-day span a range of trial frequency offsets,  $\pm 3.5$  cycles day<sup>-1</sup>, from the model frequency was searched. For each trial frequency offset,  $\Delta\nu_m$ , the pulse profile at the model frequency was shifted in phase by multiplying the Fourier harmonic coefficients by a phase factor  $e^{i2\pi k\Delta\phi_m}$ , where  $k$  is the harmonic number. The phase offset,  $\Delta\phi_m$ , is given by  $\Delta\phi_m = \Delta\nu_m(t - t_o)$  where  $t$  is a time within to a 2-day interval and  $t_o$  is an epoch near the center of the 2-day interval. This method is equivalent to refitting the background model plus Fourier expansion for each frequency  $\nu_0 + \Delta\nu_m$ . The best fit frequency for each 2-day interval was determined by comparing pulse profiles for different frequency offsets using the  $Z_6^2$  test (Buccheri et al. 1983) which measured the significance of the first 6 Fourier amplitudes.

The root-mean-square (RMS) pulsed flux was estimated from the best fit pulse profile as

$$F_{\text{RMS}} = \left[ \int_0^1 (F(\phi) - \bar{F})^2 d\phi \right]^{1/2} \quad (1)$$

where  $F(\phi)$  is the pulse profile at phase  $\phi$ ,  $0 \leq \phi \leq 1$ , and  $\bar{F} = \int_0^1 F(\phi) d\phi$  is the average flux. The pulsed fluxes were determined assuming an exponential energy spectrum,

$$f(E) = A \exp\left(-\frac{E}{E_{\text{fold}}}\right) \quad (2)$$

with a normalization  $A$  and e-folding energy  $E_{\text{fold}}$ .

Pulse frequencies were estimated from *RXTE* PCA data using a similar method. Since both data sets were quite short, 2000-2500 s, a model consisting of a constant background plus an  $n$  harmonic Fourier expansion in the pulsed phase model was fit to the data. In both observations, The pulsed phase model used a constant frequency, based upon BATSE measurements. This model was fit to the data for a grid of trial frequencies and numbers of Fourier coefficients  $n$ . The best-fit frequency was determined by the H-test (De Jager, Swanepoel, & Raubenheimer 1989). Background variations observed in these intervals were at low frequencies relative to the Cep X-4's pulse frequency. Deviations from the constant background model resulted in low frequency noise well outside the search range used which did not affect pulse frequency measurements.

### 2.3. Results

BATSE data from 1991 April to 1997 December were searched for outbursts from Cep X-4 using the pulse frequency and flux estimation method described in section 2.2. Two outbursts, each lasting about 2 weeks were detected in the BATSE data: the

first from 1993 June 20 - July 6 (MJD 49,158-49,174) and the second from 1997 July 3-15 (MJD 50,632-50,644). Figure 1 shows the history of pulse frequency and pulsed flux for the 1993 outburst. *ROSAT* also observed this outburst and measured a pulse frequency of  $15.0931 \pm 0.0002 \text{ Hz s}^{-1}$  (Schulz, Kahabka, & Zinnecker 1995) which agrees well with the BATSE measurements. From figure 1 one observes that Cep X-4's frequency increased significantly from 1993 June 24-28 (MJD 49,162-49,166). The frequency rate is  $\sim 10^{-12} \text{ Hz s}^{-1}$ , which may be intrinsic or due to orbital motion.

In 1997 July, Cep X-4 underwent another outburst which was detected with BATSE and *RXTE*. Figure 2 shows the history of pulse frequency as measured with BATSE and the *RXTE* PCA. The average frequency rate is  $\sim -10^{-12} \text{ Hz s}^{-1}$ , which is comparable in magnitude to the brief spin-up episode seen in the 1993 outburst. This spin-down may be intrinsic or due to orbital motion. Also shown is the pulsed flux history from 20-50 keV BATSE data and the phase averaged flux from *RXTE* ASM data. To determine the pulse frequencies from the PCA data, Standard 1 (125 ms, no energy resolution) data from 1997 July 18 (MJD 50,647) and 1997 July 25 (MJD 50,654) were used with techniques described in section 2.2. We found that the scatter in frequency measurements for different values of the number of Fourier coefficients,  $n$  (see section 2.2), was much larger than expected for Poisson noise. The best fit frequencies, with errors corrected for aperiodic noise (described below), were  $15.088 \pm 0.004 \text{ mHz}$  ( $n = 14$ ) on July 18 (MJD 50,647) and  $15.088 \pm 0.003 \text{ mHz}$  ( $n = 14$ ) on July 25 (MJD 50,654).

Excess aperiodic noise from Cep X-4 was likely the cause of the observed scatter in our frequency measurements, so we performed power spectral analyses on about 2000 s of Good Xenon data from 1997 July 18 and about 2400 s from July 25 to search for aperiodic variability. These data were binned into 125 ms time bins containing no gaps. The background in these intervals was modeled using *pcabackest*<sup>2</sup>, which estimates the background from Standard 2 data at 16 second intervals. This model was then interpolated to 125 ms resolution by polynomial fitting. Power due to the 66 s pulsations was removed by subtracting a model consisting of a 14th degree Fourier expansion in the best fit pulse frequency. Next a Fourier transform with no oversampling was performed on the

---

<sup>2</sup>In this paper for all background models, *pcabackest* version 1.5a was used with the Q6, Activation, and Cosmic X-ray models. For the fainter July 25 observation, *pcabackest* v2.0c was also tried with the L7 and 240 minute models for faint sources. Differences between the models were very small relative to source count rates, and did not significantly affect any of our results. Details of these models are available from the *RXTE* Guest Observer Facility.

background subtracted data. The Fourier coefficients  $a_k$  are given by

$$a_k = \sum_{j=1}^N (C_j - B_j) e^{i2\pi jk/N} \quad (3)$$

where  $C_j$  and  $B_j$  are the total counts and background counts in bin  $j$ ,  $N$  = the number of measurement bins, and  $i = (-1)^{1/2}$ . Equation (1) in Morgan & Remillard (1997) was used to calculate the dead-time corrected Poisson level with a time bin size of  $t_b = 125$  ms, a dead-time per event of  $\tau = 10 \mu\text{s}$ , and a dead-time window per very large event (VLE) of  $\tau_{\text{vle}} = 170 \mu\text{s}$ . In the normalization of Leahy et al. (1983), given by

$$P_{\text{Leahy}} = 2 \frac{|a_k|^2}{N_{\text{ph}}} \quad (4)$$

where  $N_{\text{ph}}$  is the total number of photons, the Poisson level is  $P_{\text{Poisson}} = 2$  for purely Poisson noise. These calculations yielded average dead-time corrected Poisson levels of  $P_{\text{Poisson}} = 1.97$  for July 18 and  $P_{\text{Poisson}} = 1.96$  for July 25. The aperiodic noise at the pulse frequency and its harmonics was estimated by averaging the source power,  $P_{\text{Leahy}}$ , in the region  $n\nu_o - \nu_o/2 \leq \nu \leq n\nu_o + \nu_o/2$ , where  $\nu_o$  is the pulse frequency ( $n=1$ ) and  $n\nu_o$  ( $n=2,3,\dots$ ) are the harmonics of the pulse frequency. This power was then compared to the average dead-time corrected Poisson level,  $\bar{P}_{\text{Poisson}}$  for each region. The errors on the frequency measurements,  $\sigma_\nu$ , listed above and shown in figure 2 include a correction due to this excess aperiodic noise, given by  $\sigma_\nu = (\bar{P}_{\text{Leahy}}/\bar{P}_{\text{Poisson}})^{1/2} \sigma_{\text{Poisson}}$ , where  $\sigma_{\text{Poisson}}$  is the error expected for Poisson noise only.

Next, we wished to measure the rms variation of the aperiodic noise component. We renormalized the power such that the fractional rms variation in source intensity over a given frequency range is related to the integral of the power in that range, i.e.

$$\frac{\sigma_S^2}{\bar{S}^2} = \int_{\nu_1}^{\nu_2} P(\nu) d\nu \quad (5)$$

where  $\sigma_S^2$  is the variance on the source count rate due to the frequency range  $[\nu_1, \nu_2]$  and  $\bar{S} = \frac{1}{N} \sum_{j=1}^N (C_j - B_j)$  is the mean source count rate. The power spectrum was then calculated by

$$P_k = (P_{\text{Leahy}} - P_{\text{Poisson}}) \frac{N_{\text{ph}} T}{\left( \sum_{j=1}^N (C_j - B_j) \right)^2} \quad (6)$$

where  $T$  is the duration of the data and  $\sum_{j=1}^N (C_j - B_j)$  is the total source counts in bin  $j$ . Figure 3 shows the power spectra, plotted as fractional power per logarithmic frequency interval, from 1997 July 18 in the top panel and July 25 in the bottom panel. In these units, a  $1/f$  power law is a horizontal line. Aperiodic variability is present in both time intervals,

with an rms variation of 17-19% ( $\nu = 0.01-1$  Hz) for both days. In the 1988 outburst, *Ginga* observed aperiodic noise with an rms variation of about 6% for the same frequency interval. The source was apparently noisier in *RXTE* observations.

Clearly evident in figure 3 is the presence of considerable low frequency noise on 1997 July 25 (bottom panel) which is not present in the top panel. We compared variations in the pulsed flux, mean background subtracted flux, and the background model (generated using *pcabackest*) to determine if these features were intrinsic to Cep X-4. The unpulsed flux and pulsed flux for July 25 were measured by fitting a constant plus a 14 harmonic Fourier expansion in the best-fit pulse frequency to intervals exactly 2 pulse periods long. The background model was binned at the same resolution and subtracted from the unpulsed flux. The variations observed in the unpulsed flux prior to background subtraction were about 3-4 times the background model variations. Figure 4 shows the background model, the background subtracted unpulsed flux, and the pulsed flux. The background subtracted unpulsed flux (denoted by the solid histogram) and pulsed flux (denoted by the dashed histogram) increased slowly to a broad peak, followed by a faster decrease. The background model (denoted by the dotted line) also slowly rose to a flat peak and then decreased, but it peaked later. The pulse fraction remained essentially constant throughout this interval, so it was unlikely that the variations observed were due to background fluctuations. On July 18, when Cep X-4 was about 2 times brighter in the ASM, the unpulsed and pulsed flux remained approximately constant during our observations. Apparently Cep X-4 was less stable at lower intensities.

Average pulse profiles were generated by epoch-folding  $\sim 10$  days of 20-50 keV BATSE CONT (2.048 s resolution data) for both the 1993 and 1997 outbursts. A quadratic frequency model fit to the observed frequencies in Figures 1 & 2 was used in the epoch-folding. Pulse profiles from 1993 June 20-29 (MJD 49,158-49,167) and 1997 July 4-14 (MJD 50,633-50,643) are shown in the top and bottom panels respectively in Figure 5. Both profiles show a large main peak (phase  $\sim 0.2 - 0.6$ ) followed by smaller second peak atop a broad shoulder (phase  $\sim 0.6 - 0.9$ ) and a valley (phase  $\sim 0.9 - 1.2$ ).

Pulse profiles from *RXTE* observations were generated by epoch-folding Good Xenon data from 1997 July 18 and July 25. Good Xenon data were binned into 125 ms bins and divided into 8 energy bands. The background in each band was estimated at 16 s intervals using *pcabackest* and interpolated to 125 ms resolution by polynomial fits. The background subtracted data were folded at the best fit frequencies from the fits to the Standard 1 data shown in figure 2. Figure 6 shows the pulse profiles from July 18 (left hand panel) and July 25 (right hand panel). The pulse profile shows energy dependent features and considerable structure with a large main peak (phase  $\sim 0.7-1.0$ ) followed by a deep notch at low energies

(phase  $\sim 1.0-1.1$ ). The notch is followed by a second peak (phase  $\sim 1.1-1.4$ ) and a valley (phase  $\sim 1.4-1.7$ ). The profiles evolve from double peaked, with a narrow notch between the peaks at low energy, to a dominant first peak (phase  $\sim 0.7 - 1.0$ ) followed by a broad shoulder. The second peak (phase  $\sim 1.1 - 1.4$ ) appears to be weaker relative to the first peak on July 25 than on July 18.

Figure 7 is a hardness ratio for July 18 given by

$$r = \frac{h + \Delta h}{s + \Delta s} \quad (7)$$

where  $h$  is the average background subtracted count rate for 9-20 keV,  $\Delta h$  is the mean subtracted pulse profile count rate for 9-20 keV,  $s$  is the average background subtracted count rate for 2-6 keV, and  $\Delta s$  is the mean subtracted profile for 2-6 keV. The errors shown are the errors on the difference  $r - h/s$ , since we are interested in where the hardness ratio deviated from the mean value,  $0.584 \pm 0.002$ . Hardness ratios show that the notch is the hardest feature and that it is surrounded by a softer double lobed feature (phase  $\sim 0.7-1.4$ ). Similar features were also seen in hardness ratios from July 25. However, the significance of these features was reduced by the lower intensity and smaller pulse fractions in these data. The root mean squared (RMS) intensities for each energy band were calculated as  $s_{\text{rms}} = (\sum_{j=1}^N (s_j - \bar{s})^2 / N)^{1/2}$ , where  $s_j$  is the background subtracted source count rate in phase bin  $j$ ,  $N = 32$  is the number of phase bins, and  $\bar{s}$  is the mean source count rate. RMS pulse fractions,  $s_{\text{rms}}/\bar{s}$  are shown in figure 8. The pulse fraction has considerable energy dependence and appears to be decreasing as the mean source intensity decreases.

The average 20-50 keV BATSE pulse profile from 1997 July 4-14 (Fig. 5, bottom panel) is very similar to the 1997 July 18 PCA profile in the 20-30 keV energy band (Fig. 6 bottom left). The source intensity was too low to allow detection of significant profile variations at energies  $> 20$  keV with either instrument. *Ginga* observed pulse shape variations with energy during the 1988 outburst. The second peak was brighter than the first at low energies (1-7 keV) and roughly equal at higher energies (13-37 keV) (Koyama et al. 1991).

### 3. Discussion

The optically identified companions for transient pulsars with periods longer than one second are all Be or Oe stars. Recent long-term studies with BATSE revealed that Be/X-ray binaries exhibit series of often periodic outbursts and most appear to have a long-term spin-up trend (Bildsten et al. 1997). One other system, A 1118-616, may be experiencing a spin-down trend, but the duty cycle for this source, like Cep X-4, is quite low. Long-term spin-down in X-ray pulsars is thought to be caused by the propeller effect (Illarionov &



Sunyaev 1975). Simple accretion theory assumes that material from the companion star is flowing onto a rotating neutron star with a magnetic field. The magnetic field is so strong that it determines the motion of the material in a region of space surrounding the neutron star called the magnetosphere. The magnetospheric radius  $r_m$ , is defined to be the distance from the neutron star at which all magnetic field lines are closed loops. Assuming a dipole field at large distances from the neutron star, the magnetospheric radius can be estimated by equating the magnetic energy density to the total kinetic energy density of the accreting gas. Therefore from Shapiro & Teukolsky (1983) ,

$$r_m = 3.09 \times 10^8 \text{ cm } \epsilon \mu_{30}^{4/7} m^{-1/7} \dot{M}_{17}^{-2/7} \quad (8)$$

where  $\mu_{30}$  is the magnetic moment of the dipole field in units of  $10^{30}$  G cm<sup>3</sup>,  $m$  is the neutron star mass in units of  $1.4M_\odot$ ,  $\dot{M}_{17}$  is the mass accretion rate in units of  $10^{17}$  g s<sup>-1</sup>, and  $0.5 \lesssim \epsilon \lesssim 1$  for disk accretion (Ghosh & Lamb 1979; Arons 1993; Ostriker & Shu 1995; Wang 1996) and  $\epsilon = 1$  for wind accretion (Shapiro & Teukolsky (1983)). When  $r_m$  exceeds the corotation radius,  $r_{co}$ , the distance from the neutron star where centrifugal forces just balance local gravity, the propeller effect is believed to occur. Matter will be ejected from the magnetic field lines when the centrifugal forces exceed gravitational force. This ejected matter gains angular momentum from the pulsar, causing it to spin down. If we assume the long-term spin-down observed in this system is due to the propeller effect, then by equating the magnetospheric and co-rotation radii, we can estimate the critical mass accretion rate where the propeller effect begins

$$\dot{M}_{\text{crit}} = 8.41 \times 10^{17} \text{ g s}^{-1} \epsilon^{7/2} \mu_{30}^2 m^{-5/3} P^{-7/3} \quad (9)$$

where  $P$  is the pulsar spin period in seconds. At this critical mass transfer rate, Corbet (1996) predicts a transition from neutron star accretion to magnetospheric accretion, accompanied by a large drop in luminosity. Using a magnetic field estimate of  $B = 2.6 \times 10^{12}$  G (Mihara et al. 1991), a distance estimate  $d = 3.8 \pm 0.6$  kpc (Bonnet-Bidaud & Mouchet 1998), a spin period of  $P = 66.25$  s, along with typical neutron star parameters  $m = 1$  and  $R = 10^6$  cm, we estimate the minimum X-ray flux for neutron star accretion,  $F_{\text{ns,min}} = 9.1 \times 10^{-12} \epsilon^{7/2}$  erg cm<sup>-2</sup> s<sup>-1</sup>, and the maximum for magnetospheric accretion,  $F_{\text{m,max}} = 3.3 \times 10^{-15} \epsilon^{7/2}$  erg cm<sup>-2</sup> s<sup>-1</sup>. In 1993 January *ROSAT* observed a quiescent 0.1-2.5 keV flux level of  $2.8 \times 10^{-13}$  erg cm<sup>-2</sup> s<sup>-1</sup> from Cep X-4 (Schulz, Kahabka, & Zinnecker 1995). This flux level fell in the gap between  $F_{\text{ns,min}}$  and  $F_{\text{m,max}}$ . Schulz et al. (1995) estimated that the *ROSAT* flux in the outburst in 1993 June was about 10% of the bolometric flux. Assuming that the Cep X-4 spectrum was unchanged during the quiescent *ROSAT* observations, we estimate a quiescent bolometric flux level of  $2.8 \times 10^{-12}$  erg cm<sup>-2</sup> s<sup>-1</sup>, which still falls in the gap, if we assume wind accretion ( $\epsilon = 1$ ). Clearly the observed flux was near the expected value for the onset of the propeller regime. The

estimated bolometric flux from the *ROSAT* observations was a factor of  $\sim 3$  below the expected value for wind accretion, which implies that the spectrum was much harder at low  $\dot{M}$ , similar to A 0535+262 (Giovannelli & Graziati 1992). Future quiescent observations at higher energies are needed to confirm this spectral hardening. For wind accretion, additional uncertainties in the predicted flux arise because when the propeller effect sets in at the neutron star’s equator, accretion still occurs at higher latitudes. Comparing the estimated bolometric flux with the predicted flux suggests that we may be observing disk accretion. However, additional uncertainties in the predicted flux arise from uncertainty in dimensionless parameter  $\epsilon$ . In both wind and disk accretion, the validity of the assumptions used to derive the predicted flux is uncertain because the physics at the onset of the propeller effect is poorly understood.

Long-term studies show that Be/X-ray transients exhibit two types of outbursts, giant outbursts characterized by high luminosities and high spin-up rates, and normal outbursts which typically are fainter, exhibit less intrinsic spin-up, and are spaced by some multiple of the orbital period. Normal outbursts appear to be associated with peristron passage in Be/X-ray transients with known orbits (Bildsten et al. 1997). The outbursts observed from Cep X–4 are most likely normal outbursts. Therefore the spacing of the 4 outbursts constrains the orbital period. We assume that the two previous outbursts in 1972 June–July (Ulmer et al. 1973) and 1988 March–April (Koyama et al. 1991) occurred at the same orbital phase (likely near periastron) as the two outbursts observed by BATSE. Outburst mid-times were calculated for each observation. Errors were assigned to each mid-time according to how well the mid-point of the outburst was known. An evenly spaced grid of orbital periods ranging from 25–10<sup>6</sup> days was searched, minimizing the following  $\chi^2$ :

$$\chi^2 = \sum_{k=1}^4 \frac{|1 - e^{i2\pi(e_k - e_0)/P_{\text{orb}}}|^2}{(2\pi\sigma_k/P_{\text{orb}})^2}. \quad (10)$$

where  $e_k$  is the mid-time of outburst  $k$ ,  $\sigma_k$  is the estimated error on  $e_k$ ,  $e_0$  is an epoch, and  $P_{\text{orb}}$  is an orbital period. A number of acceptable orbital periods, all  $\lesssim 147.3$  days, were found. Combining this result with Koyama et al. (1991), implies  $23 \text{ days} \lesssim P_{\text{orb}} \lesssim 147.3$  days.

The energy dependent pulse profile of Cep X–4 in figure 6 consists of two peaks separated by a narrow valley at low energies ( $< 6$  keV) which becomes filled in as the energy increases, until the leading peak (phase  $\sim 0.7$ – $1.0$ ) becomes dominant at energies above roughly 9 keV. This energy dependent behavior can be interpreted as the sum of two pulse components: a softer double lobed component that occupies pulse phase  $\sim 0.7$  to 1.4 in figure 6 and a narrower harder peak centered at phase  $\sim 1.05$  that is offset towards the leading peak of the softer double lobed component. The relationship between the

two components is well illustrated by the hardness ratio shown in figure 7. This energy dependent behavior is quite similar to that observed in Her X-1 (Deeter et al. 1998).

A possible interpretation of this energy dependent behavior can be made using a cyclotron backscattering scenario. In this scenario the outward bound X-rays from a given magnetic pole are divided into two main components: a hard pencil beam directed along the accretion column and an antipodally directed fan beam of backscattered radiation (Brainerd & Mészáros 1991). The fan beam is produced by outward bound photons that travel up through the accretion column until their energy equals the local cyclotron resonance energy whence they are backscattered. The backscattered photons will either strike the neutron star surface or be focused around the neutron star forming an antipodal fan beam. Softer photons scatter from higher altitudes in the accretion column and hence a smaller fraction of the backscattered photons are intercepted by the neutron star surface than is the case for the harder photons that scatter at lower altitudes. Therefore, the antipodal fan beam lobes produced by the softer photons will be wider, i.e. more “filled in” than the lobes produced by harder photons. At even higher energies, near the surface cyclotron energy and above, most photons will not be backscattered and will escape forming a pencil beam. For an appropriate angle of the magnetic axis to the spin axis and an observer positioned with a line-of-sight to the neutron star near the spin latitude of the magnetic dipole axis, a pulse profile consisting of a single hard pencil beam filling in the center of a softer fan beam from the antipodal pole will be observed.

A simple beam model consisting of a pencil beam surrounded by a backscattered fan beam was constructed to explore possible pulse profiles illustrative of a cyclotron scattering model. The pencil beam is represented by an emitting point on the neutron star surface and has a gaussian beam profile. Similarly, the fan beam is represented by an emitting point above the neutron star surface that is at the apex of a conical beam pointed toward the neutron star and has a gaussian profile for the conical beam “walls”. Gravitational light bending effects are taken into account by calculating photon trajectories from that height. In figure 9 we show an example profile that is reminiscent of the Cep X-4 profile. The five panels on the left represent the pulse profile in five different energy bands. The panels on the right show the apparent locations of the emitting point when the beams are visible. The height  $R$  of the fan beam emitting point decreases with increasing energy as  $E_c(r) = 11.6B_s \left(\frac{R_s}{R}\right)^3$  keV where  $E_c$  is the cyclotron scattering energy,  $B_s$  is the surface magnetic field strength in units of  $10^{12}$  Gauss and  $R_s$  is the radius of the neutron star. Sharp drops in the fan beam emission occur when the beam intersects the neutron star surface. Use of a more realistic extended emission region rather than a point would smooth out these sharp drops. The pencil beam increases in strength relative to the fan beam with increasing energy and contributes the shaded area to the pulse profile. The observer is

positioned such that only a single pencil beam is visible from one magnetic pole while only the fan beam from the opposite pole is visible. The pole emitting the pencil beam has been offset slightly to move the pulse phase centroid of the resulting pulse profile with respect to the pulse profile contributed by the fan beam. This is done to simulate the asymmetry observed in the Cep X–4 profile.

This research has made use of public target of opportunity PCA data obtained from the *RXTE* GOF. The quick-look ASM data on Cep X–4 were provided by the *RXTE*/ASM team at MIT and NASA/Goddard Space Flight Center.

## REFERENCES

- Argyle, R. W. 1997, IAU Circ. No. 6711
- Arons, J. 1993, ApJ, 408, 160
- Bildsten, L. et al. 1997, ApJS 113, 367
- Bonnet-Bidaud, J. M. & Mouchet, M. 1998, preprint, astro-ph/9801215, (A&A Letters, in press)
- Brainerd J. J. and Mészáros P., 1991, ApJ, 369, 179
- Buccheri, R. et al. 1983, A&A, 128, 245
- De Jager, O. C., Swanepoel, J. W. H., & Raubenheimer, B. C. 1989, A&A, 221, 180
- Deeter J. E., D. M. Scott, Boynton P. E., Miyamoto S., Kitamoto S., Takahama S., & Nagase F., 1998, ApJ, in press (July 20th issue)
- Fishman, G. J., et al. 1989, in Proc. GRO Science Workshop, ed. W. N. Johnson (Greenbelt:NASA/GSFC), 2
- Ghosh, P. & Lamb, F. 1979, ApJ, 232, 259
- Giovannelli, F. & Graziati, L. S. 1992, Sp. Sci. Rev., 59, 1
- Illarionov, A. F. & Sunyaev, R. A. 1975, A&A, 39, 185

- Jahoda, K., Swank, J. H., Giles, A. B., Stark, M. J., Strohmayer, T. E., Zhang, W. & Morgan, E. H. 1996, in SPIE 2808, EUV, X-ray, and Gamma-ray Instrumentation for Space Astronomy VII, ed. O. H. W. Siegmund & M. A. Grummin,(Bellingham: SPIE), 59
- Koyama, K. et al. 1991, ApJ, 366, L19
- Lamb, F. K., Petnick, C. J., and Pines, D. 1973, ApJ, 184, 271
- Leahy, D. A., Darbro, W., Elsner, R. F., Weisskopf, M. C., Sutherland, P. G., Kahn, S., & Grindlay, J. E. 1983, ApJ, 266, 160
- Levine, A.M., Bradt, H., Cui, W., Jernigan, J.G., Morgan, E.H., Remillard, R., Shirey, R.E., & Smith, D.A. 1996, ApJ, 469, L33
- Mihara, T. et al. 1991, ApJ, 379, L61
- Morgan, E. H., Remillard, R. A., Greiner, J. 1997, ApJ, 482, 993
- Ostriker, E. C. & Shu, F. H. 1995, ApJ, 447, 813
- Roche, P., Green, L., & Hoenig, M. 1997, IAU Circ. No. 6698
- Schulz, N. S., Kahabka, P., & Zinnecker, H. 1995, A&A, 295, 413
- Shapiro, S. L. & Teukolsky, S. A. 1983, Black Holes, White Dwarfs, and Neutron Stars, (New York: John Wiley & Sons), 450
- Ulmer, M. P. et al. 1973, L. E. 1973, ApJ, 184, L117
- Wang, Y. M. 1996, ApJ, 465, L111
- White, N. E., Swank, J. H., & Holt, S. S. 1983, ApJ, 270, 711
- Zhang, W., Jahoda, K., Swank, J. H., Morgan, E. H., & Giles, A. B. 1995, ApJ, 449, 930

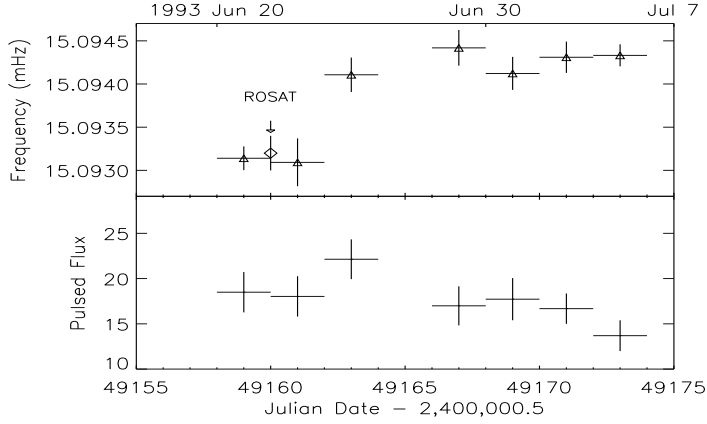


Fig. 1.— Cep X-4 pulse frequency and pulsed flux measurements determined at 2-day intervals using BATSE from 1993 June 20-July 6 (MJD 49,158-49,174). The pulse frequencies have been barycentered, but no binary correction has been applied, since the orbit is unknown. The square denotes the frequency measurement by ROSAT (Schulz, Kahabka, & Zinnecker 1995). The rms pulsed fluxes (20-50 keV) in the center panel were calculated at 2-day intervals assuming an exponential spectrum (equation 2) with  $E_{\text{fold}} = 15$  keV ( $1 \text{ mcrab} = 6.3 \times 10^{-3} \text{ keV cm}^{-2} \text{ s}^{-1}$ ).

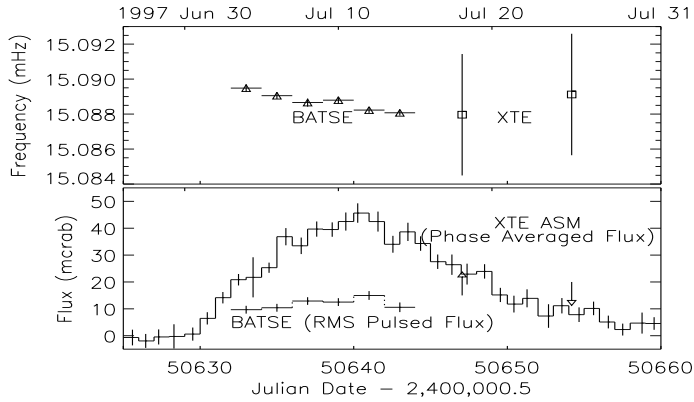


Fig. 2.— Pulse frequency and flux measurements from the 1997 July 1 - 1997 Aug 15 (MJD 50,630-50,657) outburst of Cep X-4. The pulse frequencies in the top panel, denoted by diamonds, were determined at 2-day intervals from 20-50 keV BATSE DISCLA data. These pulse frequencies have been barycentered, but no binary correction has been applied. The squares denote pulse frequency measurements from *RXTE* PCA data. The errors on the PCA frequency measurements have been corrected for excess aperiodic noise. The solid lines in the bottom panel denote rms pulsed fluxes (20-50 keV) measured at 2-day intervals with BATSE. The dotted lines are phase averaged 2-12 keV fluxes measured at 1-day intervals with *RXTE* ASM ( $1 \text{ mcrab} = 0.075 \text{ cts s}^{-1}$ .)

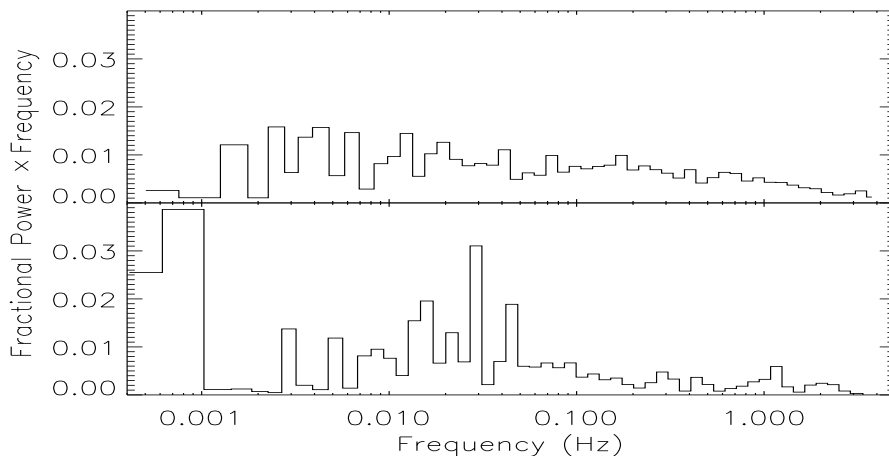


Fig. 3.— Power Spectra from 1997 July 18 (top panel) & July 25 (bottom panel) PCA observations. The mean pulse profile was subtracted from the data before calculation of the power spectrum. The Poisson level has been subtracted. The power is normalized to the mean source counts squared and has been multiplied by the analysis frequency to give the fractional variance per logarithmic frequency interval.

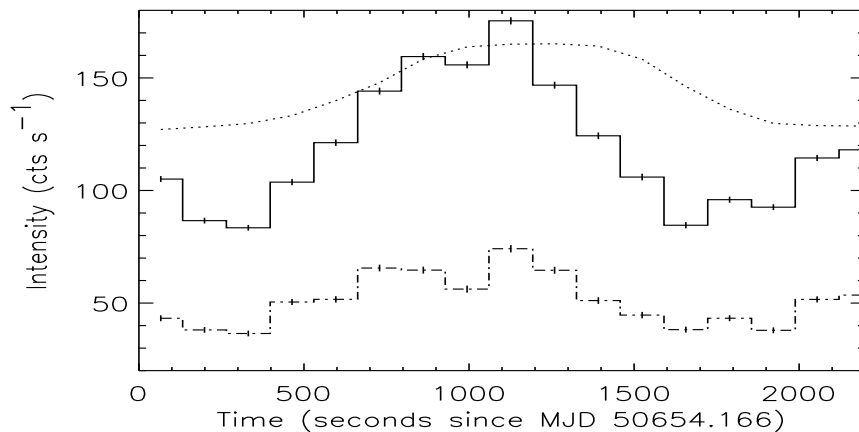


Fig. 4.— Comparison of source and background variations on 1997 July 25 (MJD 50,654). The background subtracted unpulsed flux (solid histogram), pulsed flux (dotted histogram), and background model (dotted curve) were computed for intervals exactly 2 pulse periods long. The pulse fraction is approximately constant across these observations, indicating that the observed variations in source flux are intrinsic to Cep X-4.

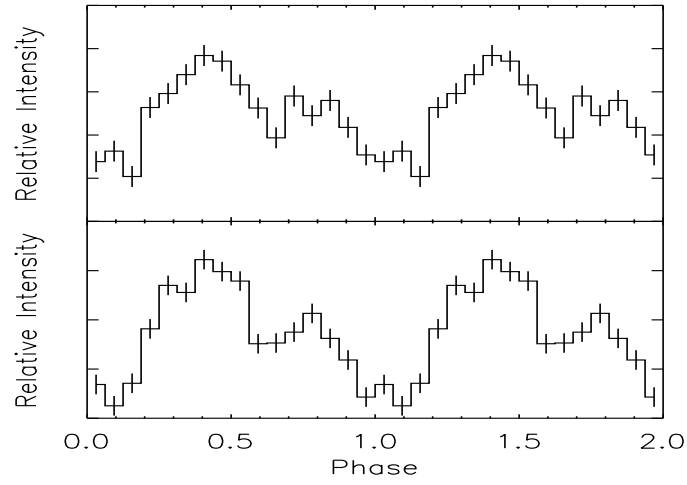


Fig. 5.— Average 20-50 keV pulse profiles from (top panel) 1993 June 20-29 (MJD 49,158-49,167) and (bottom panel) 1997 July 4-14 (MJD 50,633-50,643) BATSE data.



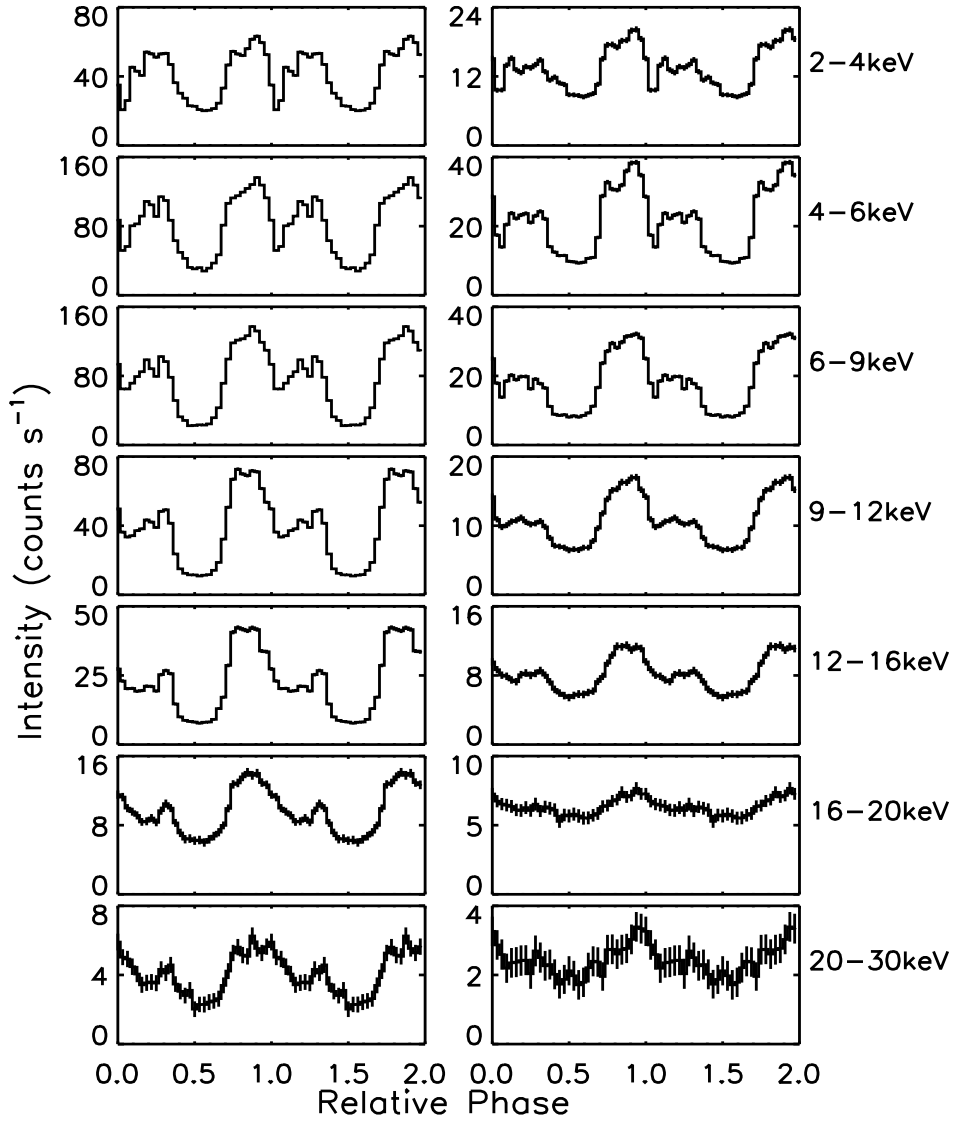


Fig. 6.— Pulse profiles from the *RXTE* PCA observations on 1997 July 18 & 25 (MJD 50,647 & 50,654).

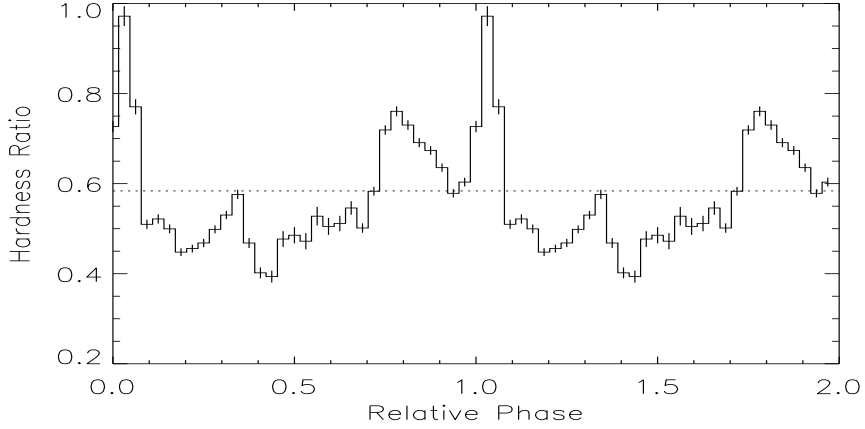


Fig. 7.— The hardness ratio between 9-20 keV background subtracted count rates and 2-6 keV background subtracted count rates on July 18 (MJD 50,647). The errors shown are errors on the difference between this ratio and the average hardness ratio. The dotted line corresponds to the average hardness ratio of  $0.584 \pm 0.002$ .

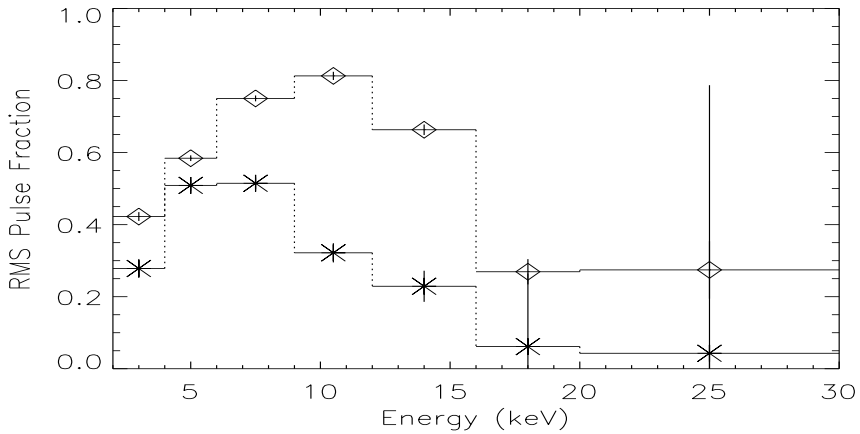


Fig. 8.— The root-mean-squared (RMS) pulse fraction from *RXTE* PCA observations on 1997 July 18 (diamonds) & 25 (asterisks). The pulse fraction is energy dependent and appears to be decreasing with intensity.

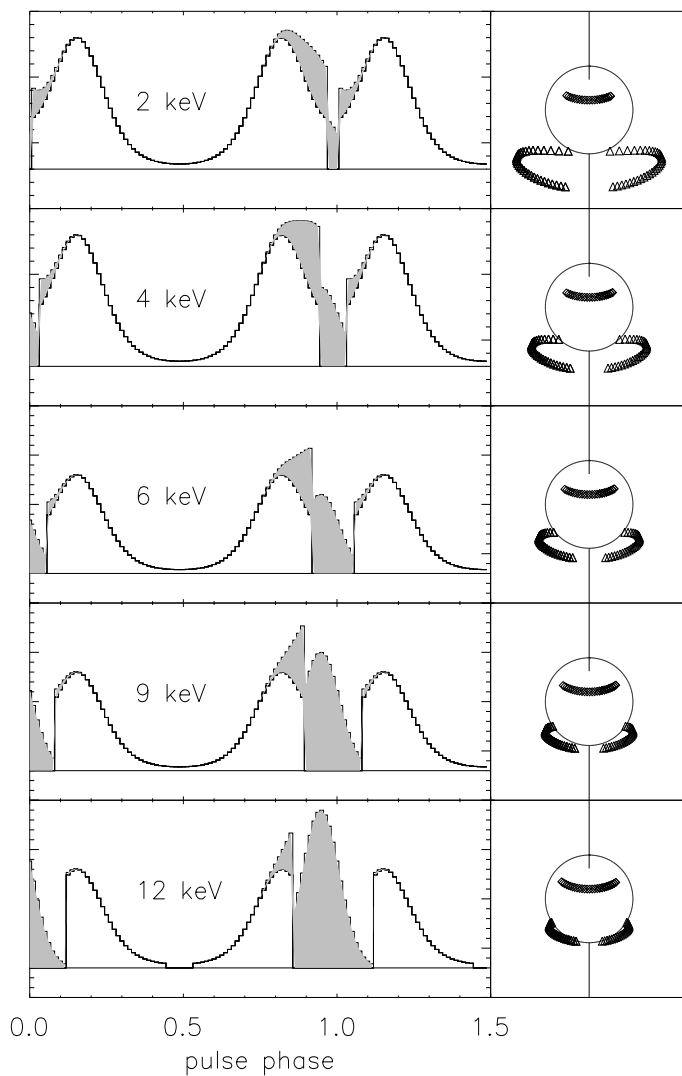


Fig. 9.— (Left panels) Pulse profiles produced by a simple cyclotron scattering beam model for the five photon energies 2, 4, 6, 9 and 12 keV (from top to bottom). The pencil beam contributes the gray shaded area to the pulse profile while the fan beam contributes a double humped profile. Artificially sharp drops in the profile (e. g. phase  $\sim 1.1$ ) result from simplified modeling of emission as from a point rather than an extended region. (Right panels) Visible locations of the points emitting the pencil and fan beam profiles. The neutron star is the circle with the spin axis shown by the vertical line. The pencil beam point is on the surface of the neutron star with the fan beam point located above the surface. The angle between the observer and spin axis is  $61^\circ$  and magnetic axis and spin axis is  $28^\circ$ .